



Experimental and numerical investigation into the corrosion performance of X100 pipeline steel under a different flow rate in CO₂-saturated produced water

Shengnan Wang¹ · Jie Zhao¹ · Yanhong Gu¹ · Dan Xiong¹ · Qunfeng Zeng² · Bin Tian³

Received: 16 February 2020 / Revised: 29 August 2020 / Accepted: 10 November 2020 / Published online: 21 November 2020
© Springer-Verlag GmbH Germany, part of Springer Nature 2020

Abstract

The effect of flow velocity on the corrosion behavior of X100 steel in CO₂-saturated produced water (CO₂-SPW) was studied. Potentiodynamic polarization (PDP) and electrochemical impedance spectroscopy (EIS) were used to study the corrosion behavior of X100 steel. X-ray diffraction (XRD), a metallurgical microscope, and a scanning electron microscope (SEM) were used to analyze corrosion product composition and morphology, respectively. The results show that the corrosion current density increases and impedance value decreases with the increase of the flow rate. The corrosion products are mainly FeCO₃ and Fe₃C. The corrosion degree of the bend segment is more serious than that of the straight segment. COMSOL simulation proposed the correlation between X100 corrosion behavior and material concentration and flow field distribution. A corrosion model was proposed, where the corrosion mechanism of X100 under simulated working condition was explained.

Keywords Dynamic corrosion · X100 · flow rate · COMSOL simulation

Introduction

The development of high-strength steel pipelines is of great economic importance to oil industry and unconventional well drilling [1–3]. As a relative new-grade pipeline steel, X100 steel has gained growing concerns recently [4, 5]. It possesses superior combination performances of strength, ductility, and corrosion resistance [6, 7]. However, the flow state in engineering is complex, the pipeline steel is normally employed under dynamic conditions [8, 9], and the

corrosion of the pipeline usually poses great threat under flow condition [10–12].

Several investigations on the dependence between the fluid velocity and corrosion rates are available in the literature [8, 13–17]. Tao Liu [18] studied the corrosion behavior of X70 in the produced water of oil field, founding that the velocity would affect the formation of corrosion product film, and the sudden change of velocity would lead to the transient pressure instability in the pipeline [19]. Mahdjet et al. [20] investigated the pitting corrosion of X100 steel by increasing the electrolyte erosion speed. The results show that pitting potentials shift towards more negative, from – 0.12 to – 0.13 V and then to – 0.17 V (SCE) with respect to corresponding zero, 3.6 m/s and 7.7 m/s of the slurry. Galvan-Martinez [5] et al. studied the corrosion kinetics of turbulent X52 pipeline steel and found that turbulence has a considerable impact on the electrochemical process on the steel surface.

The results show that the flow rate has a great influence on the corrosion behavior of steel. But the analysis of corrosion mechanism under dynamic corrosion condition is not perfect. So the method of simulation analysis is used to further supplement. Numerical simulation was used to study the effect of flow rate on corrosion except experimental studies.

✉ Jie Zhao
zhaojie@bipt.edu.cn

✉ Yanhong Gu
gu_yanhong@hotmail.com

¹ School of Mechanical Engineering, Beijing Institute of Petrochemical Technology, 19 QingyuanBeilu, Huangcun, Daxing District, Beijing 102617, China

² Key Laboratory of Education Ministry for Modern Design and Rotor-Bearing System, Xi'an Jiaotong University, Xi'an 710049, China

³ School of Material and Mechanical Engineering, Beijing Technology and Business University, Beijing 100048, China

During the process of secondary oil recovery, carbon dioxide injection technology has been widely used in order to improve oil recovery, which makes most CO₂ full of oil and gas. So a large amount of produced water is generated which contains dissolved salts, inorganic and organic constituents, solids, oil, and dissolved gases [20]. When dissolved in the aqueous phase of production water, CO₂ serves as a reservoir for the steady formation and replenishment of H₂CO₃ [21, 22]. A weak acid which attacks the surface of the steel pipeline and leads to corrosion rates higher than those observed with strong acids of similar concentrations [23]. The presence of CO₂ significantly influenced the observed electrochemical behavior of the iron dissolution reaction [24]. It led to uniform corrosion [21], local corrosion [25], stress corrosion cracking of piping steel [26], and other problems. It is particularly important to study the corrosion of high-strength pipeline steel in oilfield-produced water containing CO₂.

In this work, a dynamic simulation experiment platform was built, and configured oil-produced water with saturated CO₂ was used as the corrosion solution to simulate the flow of liquid. And the velocity is chosen as 0.2 m/s, 0.4 m/s, and 0.6 m/s. Under the experimental condition, the inner diameter of the pipeline is 50 mm; when the average flow velocity reaches 0.2 m/s, it is enough to make the liquid turbulent flow. The electrochemical test was used to analyze the corrosion of pipeline quantitatively, and the morphology and phase of corrosion products were analyzed. The dynamic experiment system was analyzed with the COMSOL software, in which the flow field and material concentration distribution in the pipeline were simulated. The corrosion initiation point was founded, and the corrosion mechanism of X100 under a simulated working condition in oil-produced water was proposed.

Experimental

Electrolyte solution

The test solution contains 18.91 g/l NaCl, 18.66 g/l CaCl₂, 0.32 g/l Na₂SO₄, 0.88 g/l MgCl₂·6H₂O, and 0.39 g/l NaHCO₃, which was used as the simulated produced water (SPW) and made from analytical grade reagents and deionized water. The mass concentration of ion is shown in Table 1. All tests were carried out at the temperature of 60 °C.

Table 1 Composition of produced water

Components	Ca ²⁺	Cl ⁻	Mg ²⁺	HCO ₃ ⁻	SO ₄ ²⁻
Mass concentration (g/l)	23.992	6.7253	0.1966	0.284.1	0.22

Dynamic corrosion test system

The study on the influence of flow velocity about internal pipeline corrosion is carried out on an independently built experimental platform to simulate the flow of liquid under working conditions [27, 28]. The picture of dynamic corrosion test system (DCTS) shown in Fig. 1a and b is the schematic diagram. DCTS includes pipeline module, control module, electrochemical test module, and gas supply module. The samples of the straight pipe section are shown in Fig. 1b ①, which is a cuboid with 5.1 cm in length, 2.2 cm in width, 0.32 cm in height, and an exposed area of 10 cm². The bend pipe section is an annulus with a diameter of 1.2 cm and an exposed area of 6 cm² (Fig. 1b ②), and the linear polarization probes (LPP) (Fig. 1b ③) are inserted into the pipeline and contacted with the fluid. The three-electrode system of the same material is widely used in engineering [29] and laboratory dynamic test system [30, 31]. The LPP [32] contains three cylindrical electrodes using the same material (X100) whose diameter is 0.5 cm and the exposed area is 5.5 cm². The gas supply module continuously provides CO₂ into the liquid tank after deoxidizing with N₂ to ensure that the CO₂ is saturating state in the liquid tank.

The experiments were conducted at the temperature of 60 °C [33] and flow rates of 0.2 m/s, 0.4 m/s, and 0.6 m/s, respectively. The flow velocity is set as the average velocity and the pipeline is turbulent flow. Before the tests, the CO₂ gas of 99.9% has been injected to the experimental container for 24 h. And CO₂ has been continuously injected to the solution during the experiments to maintain its saturation state with the pH value of 5.5. The electrochemical tests were carried out after the system runs steadily.

Material and sample

The materials used in the present work are X100 pipeline steels with a composition (wt. %) of 0.065% C, 0.95% Si, 1.69% Mn, 0.015% P, 0.002% S, 0.04% Cr, 0.27% Mo, 0.030% Ni, and Fe balance.

All the specimens were abraded with 800# to 1500# grit silicon carbide paper and polished with 2.5 and 1.5 μm diamond suspensions. Then, the samples were ultrasonically degreased and dehydrated with alcohol. The sample was immersed in a Nital etchant (4 ml of nitric acid and 96 ml of anhydrous ethyl alcohol) and treated with alcohol swapping and dried in an air stream. The microstructure of X100 in optical micrographs, as shown in Fig. 2, consists of upper bainite and granular bainite, as well as the second phase of martensite austenite [33, 34].

Electrochemical and surface-analysis tests

All the electrochemical measurements were recorded using IM6 Potentiostat. Dynamic experiment was carried out in

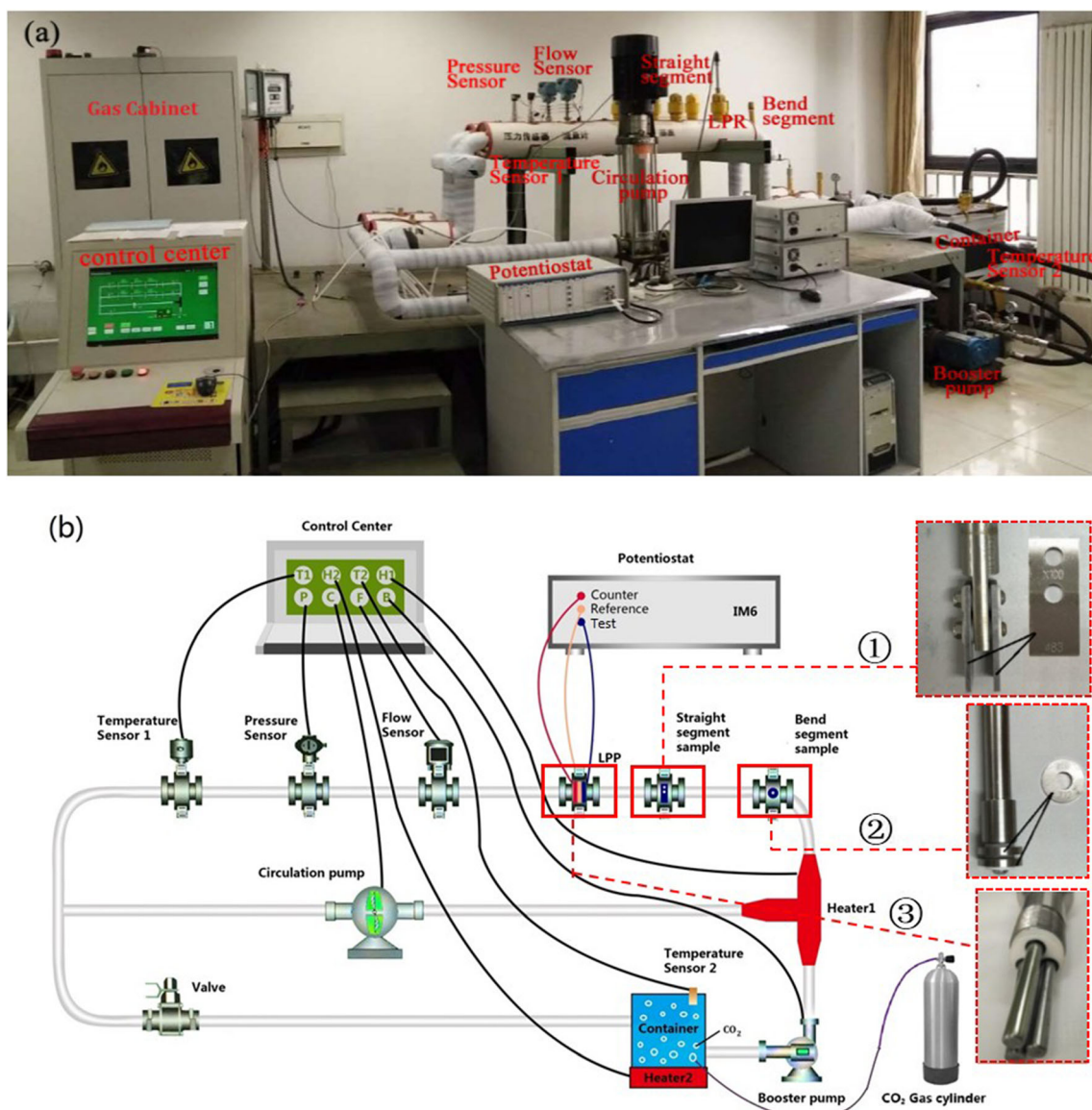


Fig. 1 (a) Picture of dynamic corrosion test system. (b) Schematic diagram of the dynamic corrosion test system with installation diagram of samples for ① straight segment, ② bend segment, and ③ linear polarization probes (LPP)

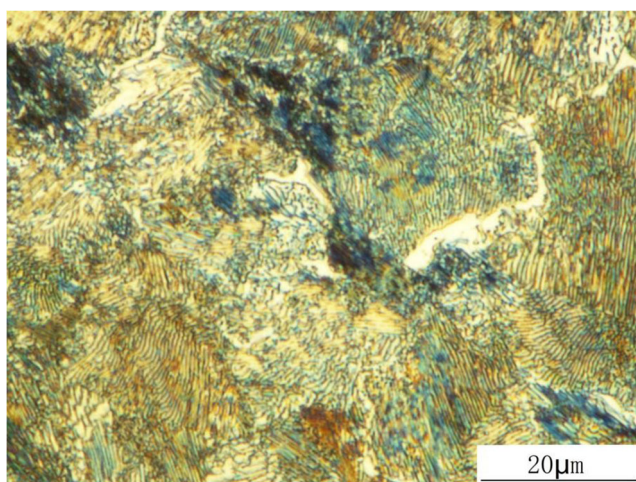


Fig. 2 Microstructure of X100 as received

DCTS. Dynamic electrochemical measurements were performed by the method of linear polarization resistance (LPR); LPR technology has been widely used in the study on dynamic corrosion of instantaneous corrosion rate [29]. The scanning range of polarization curve is set from -30 to $+30$ mV with the scanning rate of 0.5 mV/s under the simulated operating conditions. Dynamic electrochemical measurements include potentiodynamic polarization (PDP) and electrochemical impedance spectroscopy (EIS), and EIS measurements were executed with a sinusoidal potential excitation of 10 mV amplitude in the frequency range from 10^{-2} to 10^5 Hz.

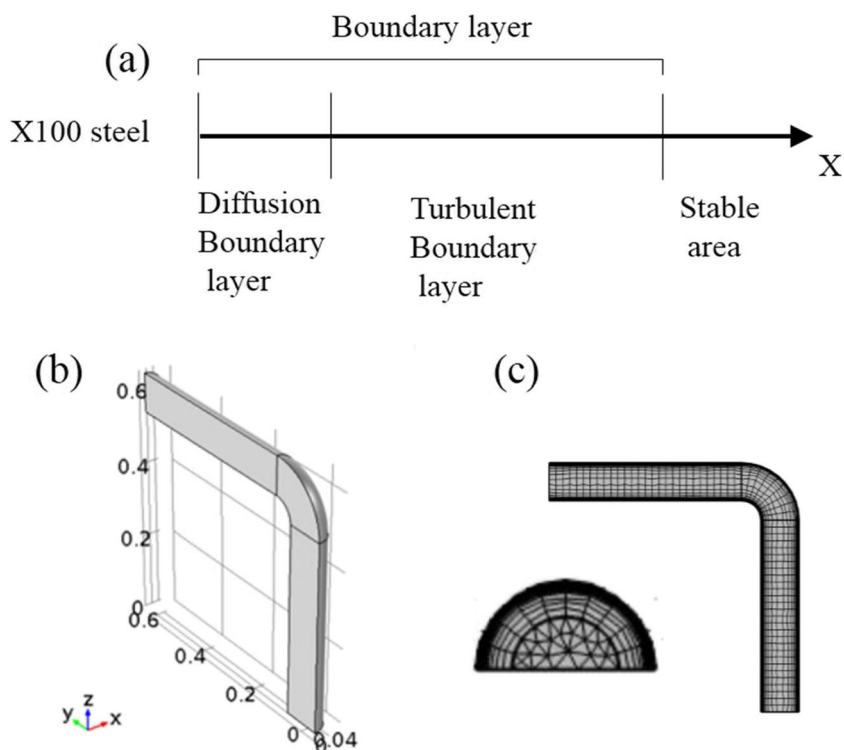
A Nikon EPIPHOT 300 series optical microscope (OM), an X-ray diffractometer (XRD) (D8 FOCUS), and an SSX-

550 scanning electron microscope (SEM) were used for imaging and chemical composition analysis.

Numerical modeling

COMSOL Multiphysics was employed to perform the flow state of saturated CO₂-produced water at different flow rates. A one-dimensional linear model as shown in Fig. 3a is established simultaneously to study the material transfer in the boundary layer region at different flow rates. As shown in Fig. 3b, a geometric model with the junction of straight pipe section and bent pipe section as the main feature is established. Since plane Y-Z is symmetric, only half of the pipes need to be calculated after modeling. According to the dynamic experimental system, the inner diameter of the pipe is 50 mm, the curvature radius at the 90° bend section is 0.1 m, and the length of the vertical and horizontal pipe sections in the model is 0.5 m. As shown in Fig. 3c, the grid division uses the layer grid commonly used in the pipeline fluid. The grid density at the wall is refined, and that near the wall is regular processing. The triangular grid is used in the center of the pipeline. Semi-empirical prediction model method is adopted in this simulation. The fluid was assumed to be incompressible, and a $k-\omega$ turbulent model (double-equation model) was used to numerically solve the simulation.

Fig. 3 Geometric model used in COMSOL simulation



Results and discussion

As the reference electrode and working electrode used in the simulated working condition are both X100 materials, so when the OCP values are close to zero, the system is stable last for 30 min.

Potentiodynamic polarization scans

Figure 4 shows the polarization curves measured after just immersing and immersing for 24 h in the CO₂-SPW under different flow rates. The polarization curve is fitted to corrosion current density (I_{corr}) by linear polarization method, and the fitting results are shown in Table 2. The current densities were 666 $\mu\text{A}/\text{cm}^2$ at 0.2 m/s, 1701 $\mu\text{A}/\text{cm}^2$ at 0.4 m/s, and 2152 $\mu\text{A}/\text{cm}^2$ at 0.6 m/s, which were increased in the wake of the increasing of the flow rate.

After soaking for 24 h, the current densities were 1337 $\mu\text{A}/\text{cm}^2$ at 0.2 m/s, 1803 $\mu\text{A}/\text{cm}^2$ at 0.4 m/s, and 3260 $\mu\text{A}/\text{cm}^2$ at 0.6 m/s. The increase of immersion time leads to an increase in corrosion current density.

Electrochemical impedance spectroscopy

Figure 5 shows the Nyquist and Bode plots of X100 in CO₂-SPW at different flow rates. The shape of impedance spectrum is similar at different flow rates, indicating that the corrosion

Table 2 PDP fitting results

Immersed time (h)	0 (just immersed)			24		
	0.2	0.4	0.6	0.2	0.4	0.6
Flow (m/s)	0.2	0.4	0.6	0.2	0.4	0.6
I_{corr} ($\mu\text{A}/\text{cm}^2$)	666	1701	2152	1337	1803	3260

mechanism is not changed by the change of flow rate, and the corrosion is mainly controlled by adsorption. As shown in Fig. 5a1 and b1, the capacitive reactance arc radius decreases with the increase of the flow rate after just immersion and immersed for 24 h, indicating that the polarization resistance decreases with the increase of the flow rate in the experimental range. There is an inductive semicircle in the low-frequency range, and it should be related to adsorbed intermediate product formed during the dissolution of X100 steel. Adsorption is maintained by intermediates of iron dissolved in a multistep reaction [35]. It can be seen that the inductive semicircle in the low-frequency range is not obvious at 24 h, which indicates that the sample adsorbs less substances, and the corrosion product film is destroyed after 24 h.

In the impedance diagram of Bode of just-immersed samples Fig. 5a2, the impedance modulus values ($|Z|$) of different samples at 0.01 Hz can be obtained, of which $|Z|_{0.2} > |Z|_{0.4} > |Z|_{0.6}$. The order of the impedance values affected by the flow velocity after 24 h immersion (Fig. 5b2) is the same order as that of just immersed, but the values are lower than that of just soaked. In order for further quantitative analysis, EIS data of different samples are fitted.

The equivalent circuit is shown in Fig. 6, in which the EIS results after just immersing were fitted by Fig. 6a, and the EIS results after immersing for 24 h were fitted Fig. 6b. R_{soln} is the solution resistance; C_{dl} is capacitance of double-charge layer; C_{cp} is the capacitance of corrosion product film; R_{ct} is charge transfer resistor; R_{cp} is the resistance of the corrosion product film. R_L is the inductance resistance, and L is the inductance. The results are shown in Table 3; the charge transfer resistance

(R_{ct}) and polarization resistance ($R_{ct} + R_{cp} + R_L$) are consistent with the arc radius and the polarization results of Nyquist capacitive reactance [35]. Due to higher electrolyte conductivity, simulated condition R_{soln} value is very small, less than $5 \Omega \cdot \text{cm}^2$.

As shown in Table 3, the $R_{ct} + R_{cp} + R_L$ was $19.9 \Omega \text{ cm}^2$ at 0.2 m/s, $18.1 \Omega \cdot \text{cm}^2$ at 0.4 m/s, and $12.8 \Omega \text{ cm}^2$ at 0.6 m/s after just immersing. The $R_{ct} + R_{cp} + R_L$ was $16.5 \Omega \cdot \text{cm}^2$ at 0.2 m/s, $14.1 \Omega \text{ cm}^2$ at 0.4 m/s, and $10.9 \Omega \text{ cm}^2$ at 0.6 m/s after 24 h. The polarization resistance decreases with the increase of the flow velocity whether just soaked or soaked for 24 h, which indicates that the impact of liquid flow is large under the simulated working condition, and is not conducive to the formation of corrosion product film on the substrate surface.

Corrosion product analysis

Macroscopic morphologies

The macrostructure of X100 after 24 h immersion in CO_2 -SPW at different flow velocities is shown in Fig. 7. Figure 7a1, a2, and a3 represent the straight pipe section; Fig. 7b1, b2, and b3 represent the elbow section; it can be clearly seen that the corrosion product coverage area of the straight pipe section surface is less than that of elbow section. In general, due to the turbulent liquid flow in the pipe bend under simulated conditions, the erosion on the surface of the specimen is more serious. Compared with the effect of different velocity on the corrosion degree of the samples, a small amount of bright metal matrix can still be seen in the straight pipe section and the bent pipe section at 0.2 m/s. At 0.4 m/s, the exposed substrate surface of straight section is no longer bright, and a thin layer of corrosion products is formed in the bend section. At 0.6 m/s, the matrix can no longer be observed, and the product film accumulated by corrosion products is thicker and more uneven.

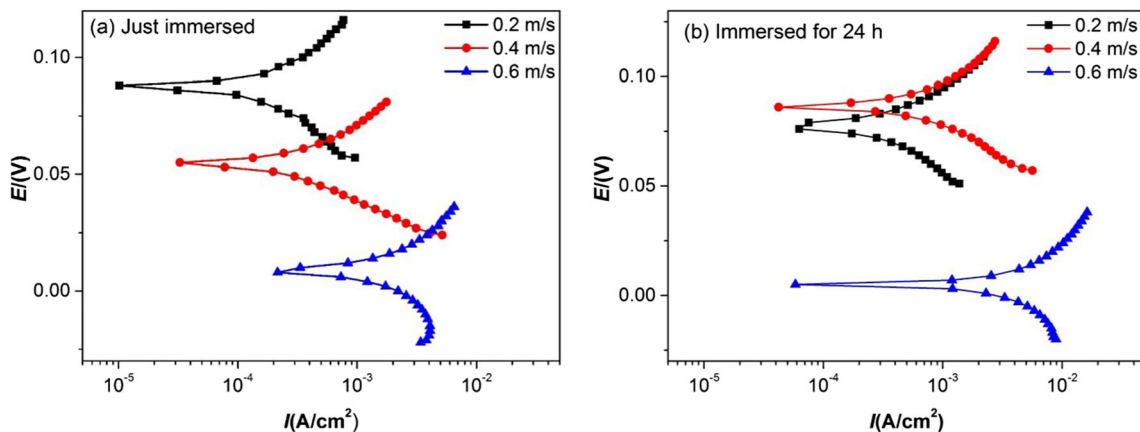


Fig. 4 Potentiodynamic polarization of X100 in CO_2 -SPW under a simulated working condition at 0.2, 0.4, and 0.6 m/s

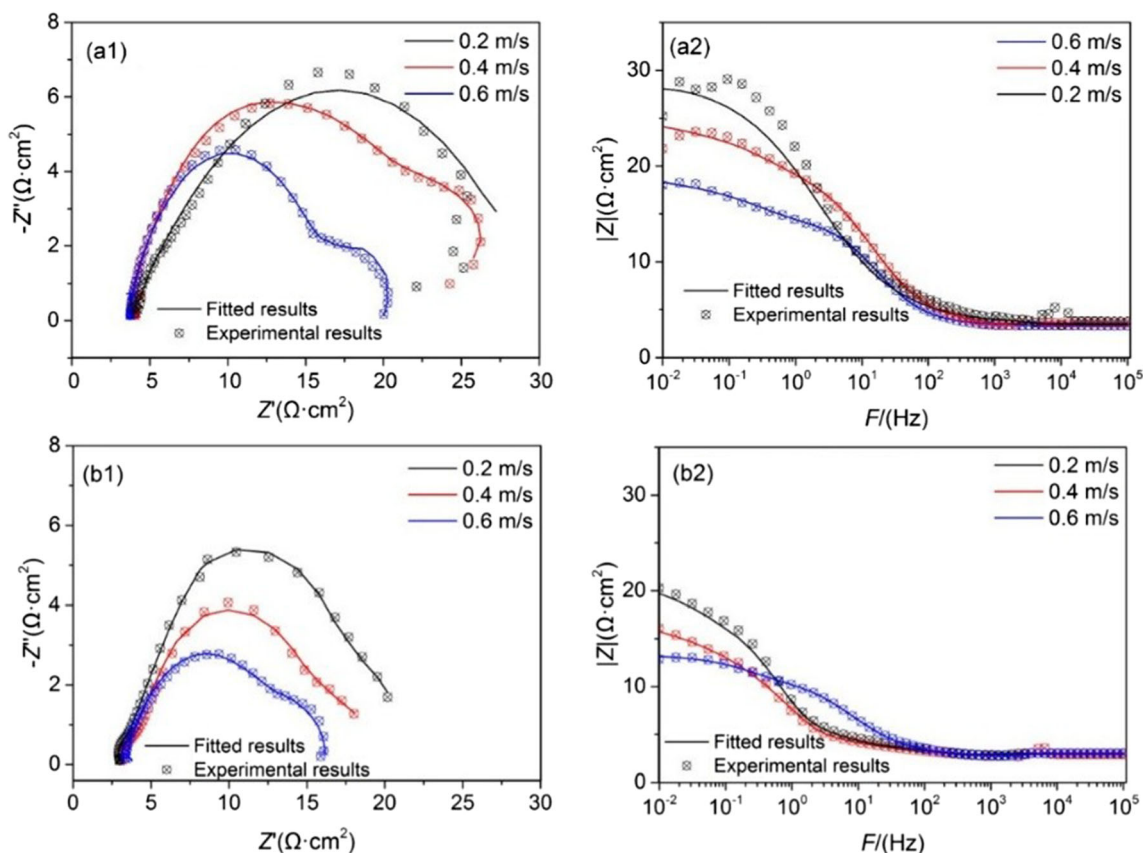


Fig. 5 EIS plots of X100 in CO₂-SPW under a simulated working condition at the flow rates of 0.2, 0.4, and 0.6 m/s: Nyquist impedance representation, (a1) for just immersed and (b1) for immersed for 24 h; impedance module representation plots (a2) for just immersed and (b2) for immersed 24 h

Microstructure

Figure 8 shows the SEM images of the corroded samples for 24 h. Figure 8a1, a2, and a3 show the images of the straight section. As shown in Fig. 8a1, the corrosion products on membrane surface are relatively loose but relatively flat at the velocity of 0.2 m/s. Compared with that in Fig. 8a1, the

corrosion products at the velocity of 0.4 m/s are relatively dense, but poor flatness is found in Fig. 8a2. However, the corrosion products appear relatively dense, but uneven topography is found in Fig. 8a3 at the velocity of 0.6 m/s.

In Fig. 8b1, b2, and b3, discrete holes (local corrosion) appear, and the corrosion product film is relatively dense with the increase of flow velocity in the bend pipe section, but it is stripped seriously because of local corrosion aggravated by turbulent scouring. So, the corrosion degree in the bend pipe section is more serious than that in the straight section.

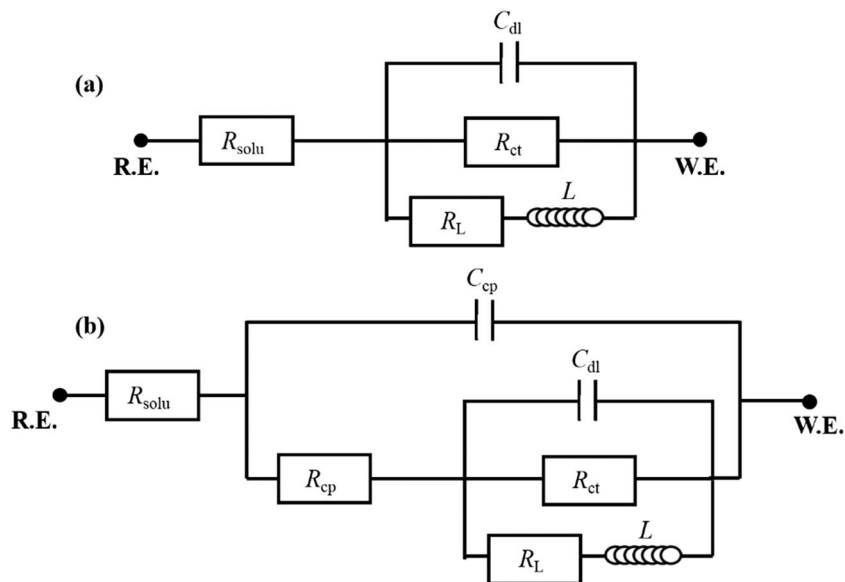
Table 3 Fitted impedance parameters of X100 just immersed and have been immersed for 24 h in dynamic CO₂-SPW of different flow rates

Components	Just immersed			Immersed for 24 h		
	0.2 m/s	0.4 m/s	0.6 m/s	0.2 m/s	0.4 m/s	0.6 m/s
$R_{\text{soln}} (\Omega \cdot \text{cm}^2)$	4.58	4.2	3.73	3.38	3.41	4.25
$C_{\text{cp}} (\mu\text{F}/\text{cm}^2)$	-	-	-	9.27 m	8.7 m	611 μ
$R_{\text{cp}} (\Omega \cdot \text{cm}^2)$	-	-	-	2.3	1.8	1.6
$C_{\text{dl}} (\text{mF}/\text{cm}^2)$	346 μ	705 μ	773 μ	1.69 m	1.58 m	111 u
$R_{\text{ct}} (\Omega \cdot \text{cm}^2)$	15.59	12.58	8.7	10.27	8.67	6.96
$R_{\text{L}} (\Omega \cdot \text{cm}^2)$	4.31	5.52	4.10	3.93	3.63	2.34
$L (\text{H} \cdot \text{cm}^2)$	1.32	1.83	1.26	2.51	1.81	1.79

XRD analysis

Figure 9 shows the XRD phases of straight segment (a) and bend segment (b). It shows that the CO₂ corrosion products of pipeline steel are mainly FeCO₃ and Fe₃C [36]. It should be pointed out that Fe₃C is not the corrosion product but the remainder of carbon steel after the preferential dissolution of ferrite [8, 14]. CaCO₃ is the most scale observed in oil production system and often exists as mixed carbonates. Precipitation happens when their saturation degree is greater than unity [37]. FeCO₃ and CaCO₃ have the same unit cell

Fig. 6 Equivalent circuits used for fitting EIS results of X100 just immersed (a) and have been immersed for 24 h (b) in CO₂-SPW



type and similar cation radii and can co-exist in a solid solution. Ca can replace Fe in the crystal structure of FeCO₃ and form a mixed substitution solid solution, as Fe_{1-x}Ca_xCO₃ [38].

Numerical modeling and corrosion model

The flow type in this model is viscous incompressible isothermal steady flow, and the effect of gravity can be ignored. When the temperature $T = 60\text{ }^{\circ}\text{C}$, the density and viscosity

of water are $\rho = 982.673\text{ kg/m}^3$ and $\mu = 4.688 \times 10^{-3}\text{ Pa}\cdot\text{s}$, respectively. When the average velocity at the entrance is $U_{\text{avg}} = 0.2\text{ m/s}$ on the cross section of the pipeline, the value of Reynolds number is as follows (Eq. 1):

$$\text{Re} = \frac{\rho U_{\text{avg}} D}{\mu} = 2.1 \times 10^4 > 4000 \tag{1}$$

The one-dimensional model does not take into account the variation along the length direction of the pipe and only considers the interaction between various substances and steel in

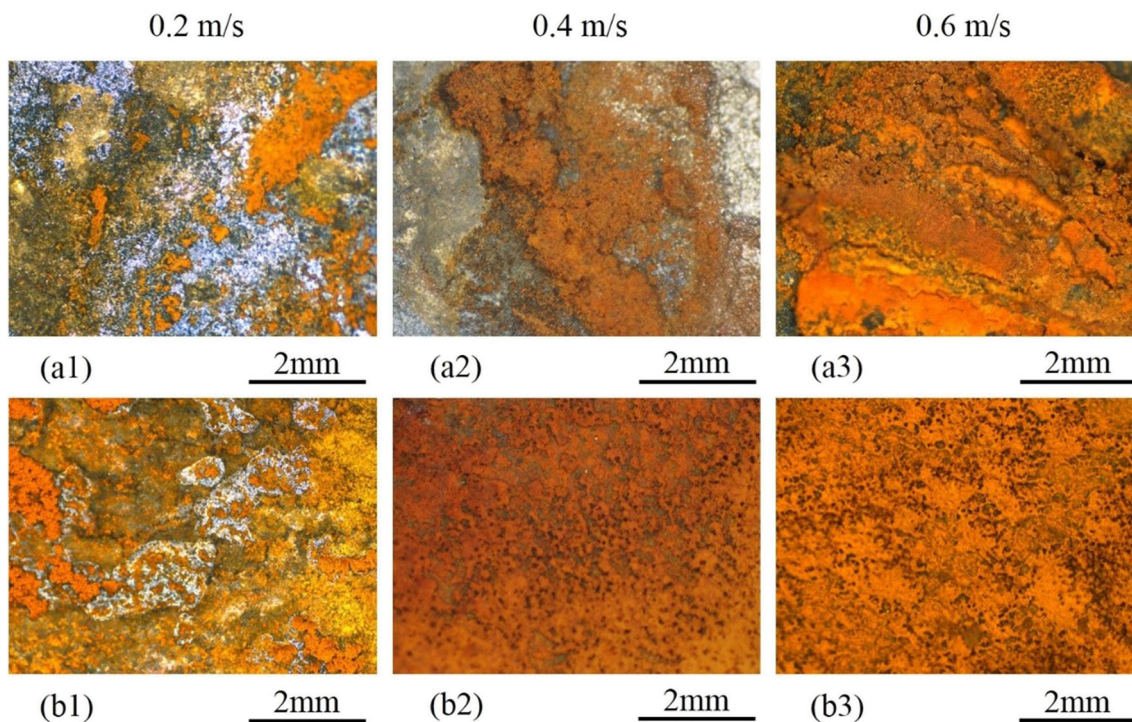
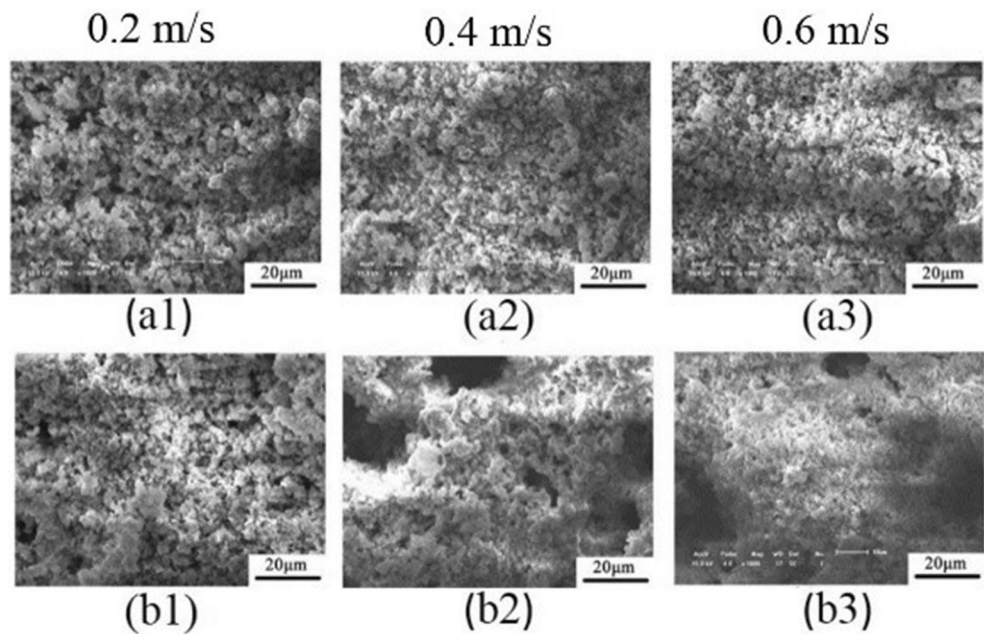


Fig. 7 Image of X100 immersed in dynamic straight segment (a1–a3) and bend segment (b1–b3) CO₂-SPW at 0.2, 0.4, and 0.6 m/s for 24 h

Fig. 8 Micrographs of X100 immersed in dynamic straight segment (a) and bend segment (b) CO₂-SPW at 0.2, 0.4, and 0.6 m/s for 24 h



the boundary layer near the surface of the steel. The geometric model is shown in Fig. 3a. The thickness of boundary layer depends on Reynolds number, and the formula is shown in Eq. 2. The variation of diffusion boundary layer and turbulent boundary layer is related to mass transfer parameters.

$$\delta = 25 * Re^{-\frac{7}{8}} * D \quad (2)$$

The δ is the thickness of the boundary layer, D is the diameter of the pipeline, and Re is the Reynolds number.

Using the electrical analysis module in COMSOL, it is assumed that all substances are dissolved in water and the transport of substances is simulated by diffusion. Considering three hydrolytic ionization reactions, three reduction reactions, and iron dissolution reactions in CO₂ aqueous solution, there are seven substances in the model, and the diffusion coefficients of each substance are shown in Table 4.

The hypothetical equation for the properties of mass transfer is:

$$\nabla \cdot (-D_i \nabla c_i) = R_i \quad (3)$$

$$N_i = -D_i \nabla c_i \quad (4)$$

D_i is the diffusion coefficient of components, c_i is the concentration of components, R_i is the consumption of chemical reactions, and N_i is the flux of materials.

According to the conservation of matter, the following formulas are:

$$-n \cdot N_i = 0 \quad (5)$$

The turbulent boundary layer is treated by adding the turbulent diffusion term D_t to the diffusion coefficient, which depends on the velocity, viscosity, density, and distance from the steel surface.

$$D_t = 0.18 * \left(\frac{x}{\delta}\right)^3 * \frac{\mu}{\rho} \quad (6)$$

The diffusion coefficient of substance is treated as the sum of the initial diffusion coefficient and turbulent diffusion term:

$$D_i = D_{i0} + D_t \quad (7)$$

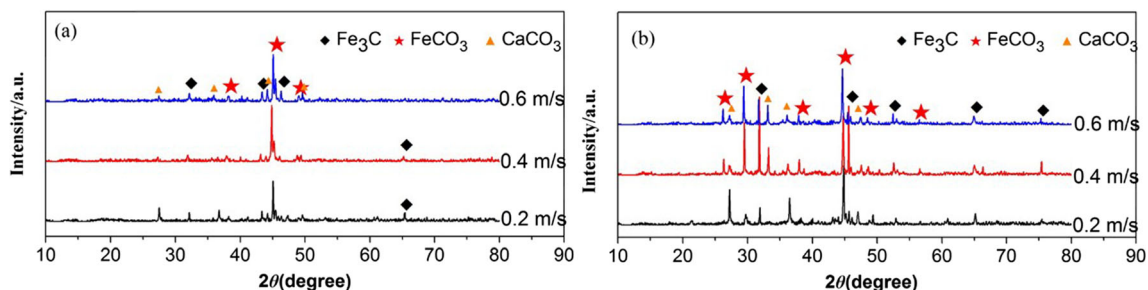
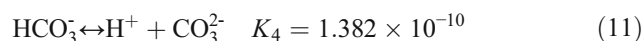
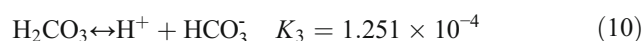
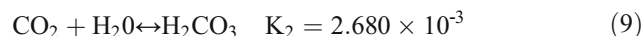
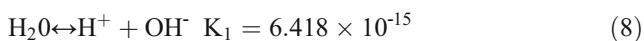


Fig. 9 XRD of X100 immersed in CO₂-SPW under the straight segment (a) and the bend segment (b) condition at 0.2, 0.4, and 0.6 m/s for 24 h

Table 4 Modeled species with their respective diffusion coefficients

Substance	CO ₂	H ₂ CO ₃	HCO ₃ ⁻	CO ₃ ²⁻	H ⁺	OH ⁻	Fe ²⁺
Diffusion coefficient (m ² /s)·10 ⁻⁹	1.96	2.00	1.11	0.92	9.31	5.26	0.72

Equilibrium reactions and equilibrium constants in the system are as follows:

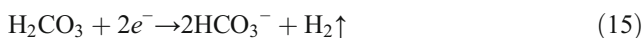


The hypothetical equation of equilibrium reaction is:

$$K_{eq} = \frac{\prod_{i \in \text{product}} (c_i/c_{a0})^{v_i}}{\prod_{i \in \text{reactant}} (c_i/c_{a0})^{-v_i}}$$

In the formula, K_{eq} is the equilibrium constant of each reaction, c_i is the concentration of substance, c_{a0} is the unit active concentration, and v_i is the corresponding chemical equivalent coefficient. The equilibrium constant K_{eq} is a function of temperature T . The electrochemical reactions on the steel surface are as follows:

The anodic reaction is the dissolution of Fe:



The initial concentration of CO₂ is

$$C_{CO_2} = K_{CO_2} * P_{CO_2} \quad (16)$$

Among them, K_{CO_2} is the Henry constant of CO₂, whose value is related to temperature, and P_{CO_2} is the partial pressure of CO₂.

Figure 10 shows the relationship between the concentration changes of each substance from the steel surface distance at a different flow velocity. In this figure, the concentration lines of H⁺, OH⁻, H₂CO₃, and CO₃²⁻ coincide with the concentration of most areas in the solution. The concentration of Fe²⁺ on the surface of the matrix is higher than that in most areas of the solution due to the dissolution of steel. In the cathodic reaction, as a result of the hydrolysis equilibrium reaction, H₂CO₃ reacts as the reactant and HCO₃⁻ reacts as the product; the concentration of HCO₃⁻ is higher than that in most areas of the solution. At the same time, owing to the continuous dissolution of CO₂ and the constant concentration of H₂CO₃, the main form of reaction is CO₂ consumption as a result. Due to the hydrolysis equilibrium reaction of HCO₃⁻, it can buffer the change of pH. The concentration of H⁺ and OH⁻ in the solution does not change with the change of distance from the steel matrix; that is, the pH of boundary layer will not change thanks to the chemical reaction. Take the concentration difference of Fe²⁺ as an example: the concentration difference of c (Fe²⁺) is 0.09 mmol/l, as the flow velocity is 0.2 m/s (Fig. 10a); the concentration difference is 0.05 mmol/l, as the flow velocity is 0.4 m/s (Fig. 10b); the concentration difference is 0.035 mmol/l, as the flow velocity is 0.6 m/s; according to Eq. 1, when the flow velocity changes, the Reynolds number changes, and the boundary layer thickness changes (Eq. 2); Figure 10 also verifies that when the flow velocity increases, the thickness of boundary layer also turned from 0.2 to 0.1 mm and finally to 0.08 mm. It can be seen that the increase of the flow velocity in the pipeline can be attributed to the closer concentration of the boundary layer area and most of

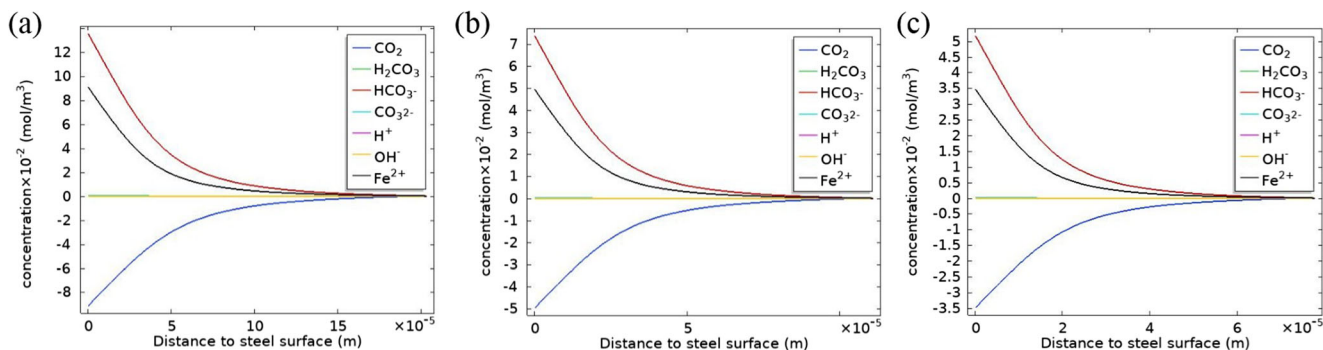


Fig. 10 Concentration difference between substance concentration in the boundary layer and solution at different inlet velocities

the desorbed concentration in the solution, which is conducive to the mixing of substances, reducing the polarization of concentration difference and promoting the chemical reaction.

The flow in the experimental pipeline is turbulent. The k - ω turbulence model which is more accurate for the near-wall region is selected in the simulation. The model equation is shown in Eqs. (17)–(22) [39, 40]:

$$\rho(u \cdot \nabla)u = \nabla \cdot [= pI + (\mu + \mu_T)(\nabla u + (\nabla u)^T) + F \quad (17)$$

$$\rho \nabla \cdot (u) = 0 \quad (18)$$

$$\rho(u \cdot \nabla)k = \nabla \cdot [(\mu + \mu_T \sigma_k^*) \nabla k] + P_k - \beta_0^* \rho \omega k \quad (19)$$

$$\rho(u \cdot \nabla)\omega = \nabla \cdot [(\mu + \mu_T \sigma_\omega) \nabla \omega] + \alpha \frac{\omega}{k} P_k - \rho \beta_0 \omega^2 \quad (20)$$

$$\mu_T = \frac{\rho k}{\omega} \quad (21)$$

$$P_k = \mu_T [\nabla u \cdot (\nabla u + (\nabla u)^T)] \quad (22)$$

Each constant in the model is defined as follows: $\alpha = \frac{5}{9}$, $\beta_0 = \frac{3}{40}$, $\beta_0^* = \frac{9}{100}$, $\sigma_\omega = 0.5$, $\sigma_k^* = 0.5$, p is the pressure function, k is the turbulent energy, ω is the specific dissipation rate, μ_T is the eddy viscosity coefficient, P_k is the turbulent energy generation term, σ_k^* is the turbulent correlation coefficient, and ∇ is the Schmitt operator. The Reynolds number in the experimental conditions is about 1×10^4 , and it is assumed that the velocity distribution at the entrance follows the law of 1/7 power.

$$U = U_{\max} \left(1 - \frac{r}{R}\right)^{\frac{1}{7}} \quad (23)$$

In the formula, U_{\max} is the maximum flow velocity, and R is the radius of the pipeline. The maximum velocity obeying the 1/7 power law is about 1.2 times of the average velocity, and the multiple decreases with increasing turbulence. The flow field and mass transfer at the inlet maximum velocity of 0.2, 0.4, and 0.6 m/s are simulated and calculated. In all the input simulation parameters, the exchange current density of Fe ion

is the sensitive factor, which has the greatest impact on the simulation results.

Under the setting velocity field, the transfer of CO_2 in the pipeline is simulated without considering the chemical reaction. The diffusion coefficient D is set to $2 \times 10^{-9} \text{ m}^2/\text{s}$, and the concentration of CO_2 at the given inlet is 0.03 mmol/l. The hypothetical equation of dilute matter transfer is shown in Eqs. (24) and (25):

$$\nabla \cdot (-D_i \nabla c_i) + u \cdot \nabla c_i = R_i \quad (24)$$

$$N_i = -D_i \nabla c_i + u c_i \quad (25)$$

D_i is the diffusion coefficient, c_i is the concentration of substance, and N_i is the flux of diffusion substance.

The simulation results are shown in Fig. 11. Figure 11a, b, and c are the flow field line distribution of the turbulent, and the bend section is partially enlarged. The velocity at the top of the pipe is higher than that at the bottom of the pipe, because the direction of the flow field is forced to change due to the change of the shape of the pipe, resulting in the uneven distribution of the flow field. Due to the inertia of the fluid, the fluid particles cannot adhere to the wall immediately at the turning point, but leave the wall surface at the elbow, resulting in a vortex. Because of the continuity of fluid flow, the fluid then flows and swallows the vortex until the fluid fills the entire pipe section. In the process of analysis, it is found that the larger the velocity, the longer the duration of vortex.

In order to analyze the pressure distribution at different positions in the pipeline, ① a lower straight pipe section, ② the lower elbow section, ③ the 45° elbow section, ④ the upper elbow section, and ⑤ a upper straight pipe section are selected for analysis, as shown in Fig. 12a. Figure 12c shows the pressure distribution in the pipeline at 0.2 m/s, and the pressure distribution at section ① is uniform, and the pressure difference can be almost ignored. Due to the bending of the pipeline, the streamline will bend. Under the action of centripetal force, the pressure on the outer wall of the pipeline is higher than that on the inner wall. On the outer side of the pipe wall, the pressure increases first and then decreases, and the pressure on the inner side first decreases and then

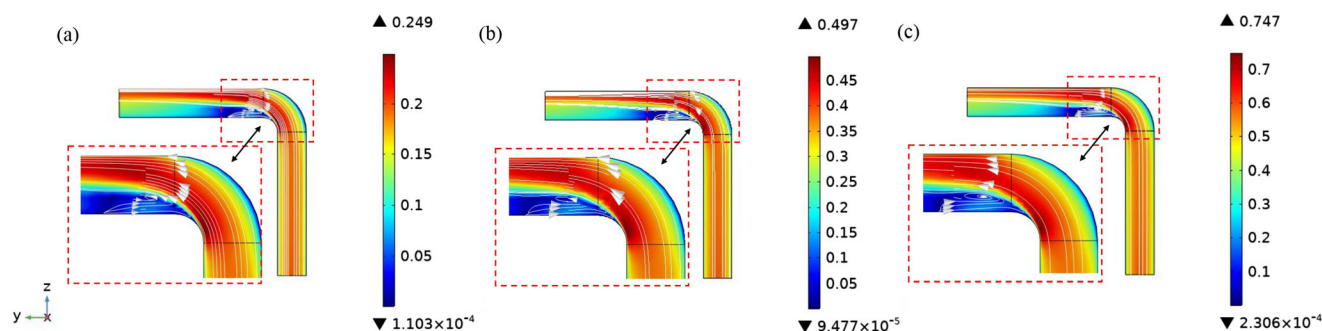


Fig. 11 Distribution of flow field at different inlet velocities 0.2 m/s, 0.4 m/s, and 0.6 m/s

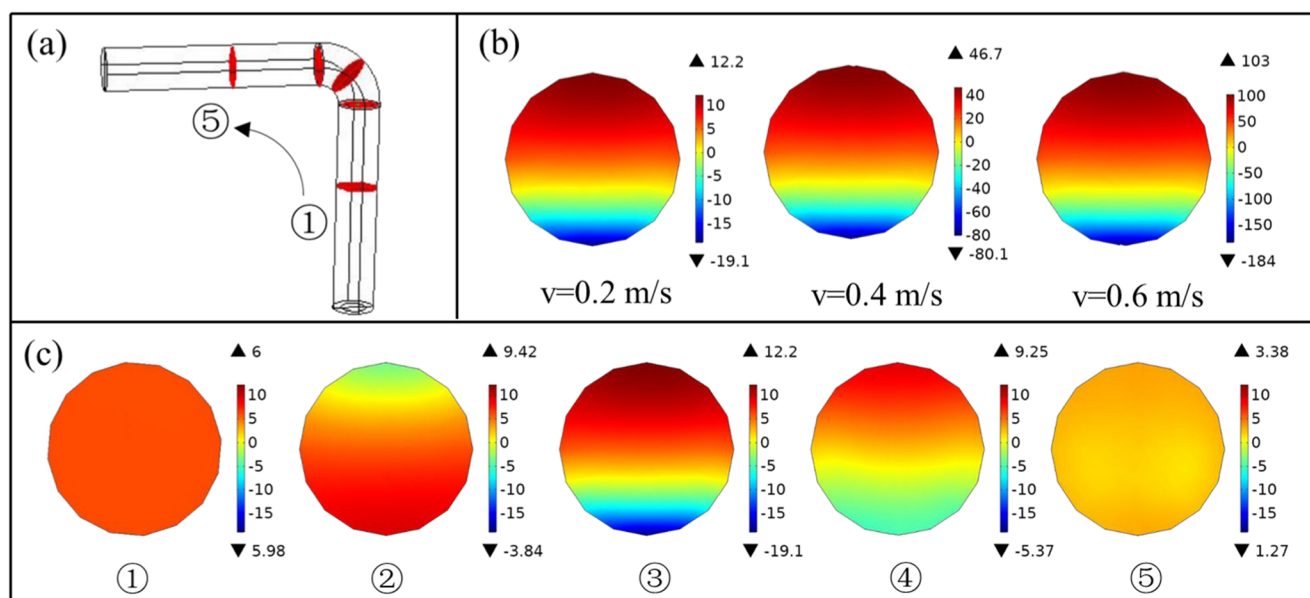


Fig. 12 Simulation results of pipeline pressure distribution. **(a)** Location of the sections. **(b)** Effect of velocity on pressure distribution of 45° cross section. **(c)** Pressure distribution at various sections

increases. Negative pressure appears at the elbow section, and the fluid flows alternately in the pipe. In the process of vortex generation and disappearance, friction, impact, and mass exchange will inevitably occur, which will consume a part of mechanical energy. Therefore, the pressure of section ⑤ is less than that of section ①. In the above sections, the pressure difference of section ③ is the largest, and the pressure difference gradually increases with the increase of flow rate, as shown in Fig. 12b.

Figure 13 shows the distribution of CO₂ concentration near the wall at different flow rates. The CO₂ concentration in the elbow section is higher than that in the straight pipe section, especially in the lower elbow, upper elbow, and vortex. When the flow rate increases, the maximum concentration turns from 0.034 and 0.036 to 0.037 mmol/l, respectively, increasing gradually. As shown in Fig. 12, changes in flow rate lead to changes in fluid internal pressure. When the pressure drops to the saturated vapor pressure of the liquid, the gas dissolved in the solution will be separated in the form of small bubbles,

resulting in cavitation. In addition, as the pressure decreases, the partial pressure of CO₂ will also change so that CO₂ is separated in the form of gas and enriched in the high flow and low pressure areas of the pipeline network. The flow rate and reactant concentration at different positions of the pipeline will affect the corrosion behavior of the pipeline. The detailed analysis results are shown in Fig. 14a and b represent the variation of CO₂ concentration and wall shear rate along the wall from the inlet to the outlet of the pipeline, respectively. In Fig. 14a, CO₂ concentration and wall shear stress are the highest at 0.5 m that is section ②. At the bend section, when the fluid flow direction is forced to change, it will cause a strong impact on the bend pipe, and the additional fluid will produce an extra force on the metal surface. The internal friction force (*F*) divided by the contact area (*S*) is the shear stress (*τ*) in the liquid [10, 41].

$$\tau = \frac{F}{S} = \frac{\mu S \gamma}{S} = \mu \gamma \tag{26}$$

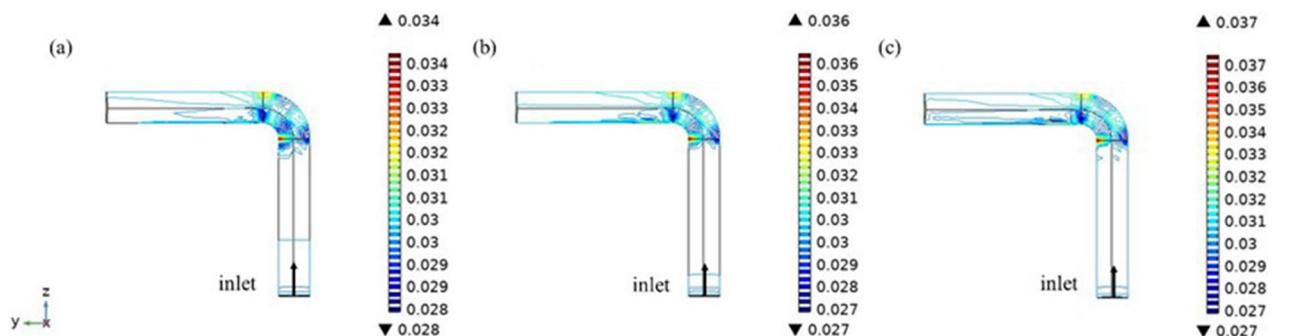


Fig. 13 Distribution of CO₂ concentration contour at different inlet velocities: 0.2 m/s, 0.4 m/s, and 0.6 m/s

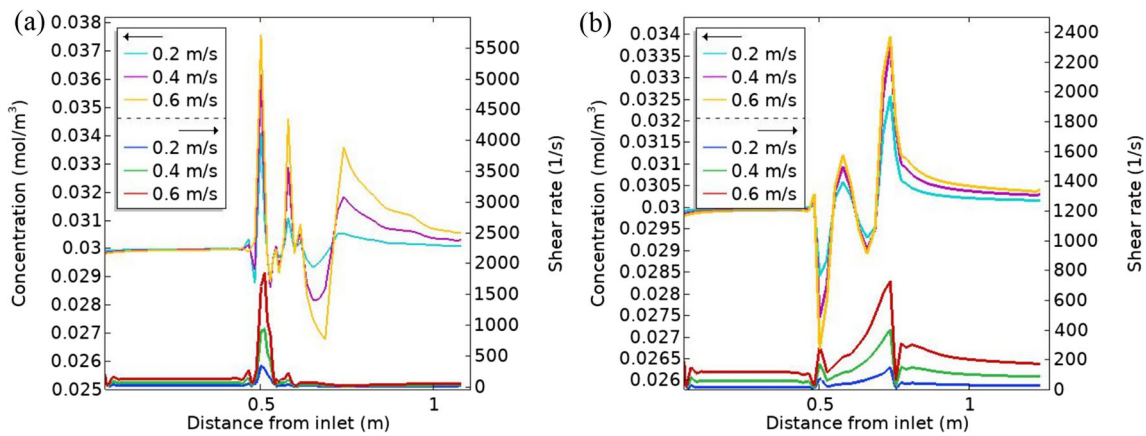
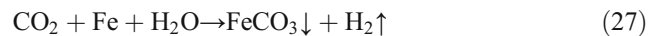


Fig. 14 Distribution of CO₂ concentration and shear stress along the pipeline. (a) Innermost side of the pipe. (b) Outmost side of the pipe

where μ is the viscosity, $4.688 \times 10^{-3} \text{ Pa} \cdot \text{s}$, and γ is the shear rate. With the increase of flow rate, the shear rate increases, and the wall shear stress turns from 1.41 to 8.44 Pa. High wall shear stress can peel off the formed corrosion product film and be carried away by the fluid. Especially, once the corrosion product film is destroyed, a damaged area appears, which a small anode becomes, and the rest of the corrosion products cover the area as a large cathode. Meanwhile, the CO₂ concentration increased; these characteristics will accelerate the local corrosion of the damaged area. Compared with Fig. 14a and b, the same corrosion-prone points appear at the upper elbow of 0.75 m, but the CO₂ concentration (c 0.0338 mmol/l) and the wall shear stress value (3.75 Pa) are less than those in Fig. 14a, so the preferred corrosion initiation point is on the inner side of the lower elbow.

Figure 15 is the corrosion model of dynamic corrosion. Figure 15a is the coupling field of flow velocity and CO₂ concentration distribution in the pipeline. The COMSOL simulation results show that the separation area of the bend segment is the easy initiation point of corrosion, therefore taking the area with red frame to discuss the corrosion process (Fig. 15b, c, d). The main equation of the reaction is as follows:



The main product is FeCO₃, accompanied by other carbonate precipitation, and Fe₃C which is left by steel dissolution forms product film together as shown in Fig. 15c. At the initial stage of corrosion, the product film can protect the matrix and slow down the corrosion. However, under the working

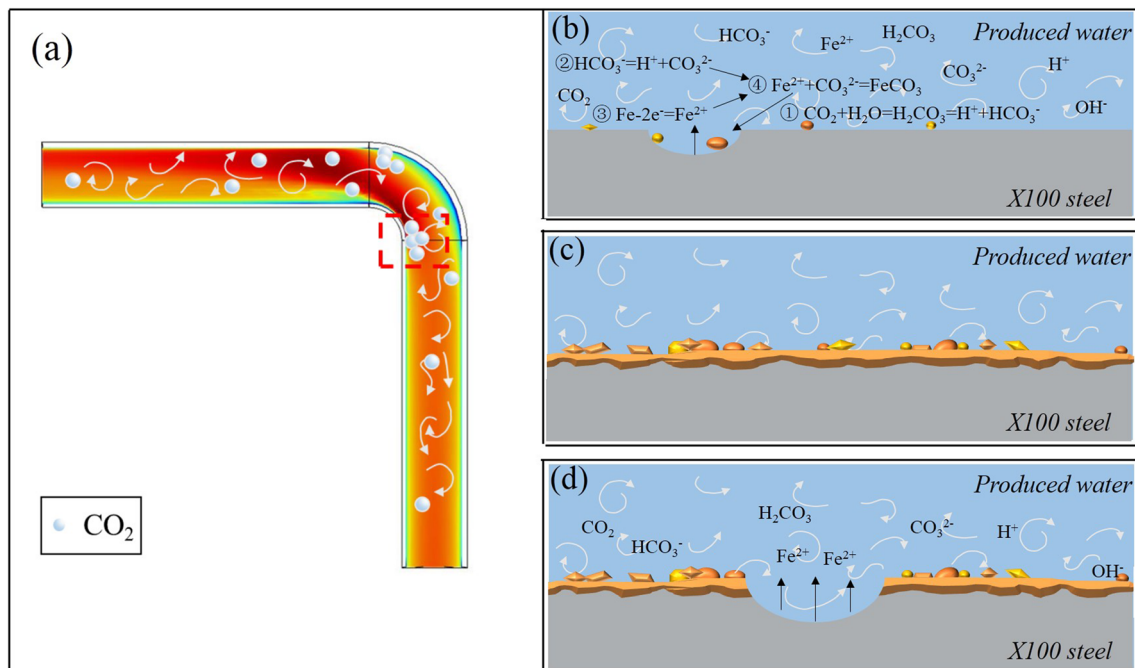


Fig. 15 Local corrosion mechanism model of X100 under dynamic conditions: (a) coupling filed of fluid velocity and concentration of CO₂ and (b), (c), and (d) the corrosion process

condition, the flow of the fluid is mainly turbulent, and high wall shear stress will lead to the spalling of the product film (Fig. 7, Fig. 8, and Fig. 15d), resulting in the metal surface exposed to the corrosive medium and strongly eroded by the fluid. The reaction of ①, ②, ③ and ④ in Fig. 15b will continuously be carried out, which leads to serious corrosion of the matrix and an increase of corrosion current density. The experimental research results under simulated working conditions have more real guiding significance for the project.

Conclusion

A simulated working condition platform was built to study the corrosion behavior of X100 steel in saturated CO₂ water. The corrosion mechanism was analyzed by using the COMSOL software as an auxiliary tool. The results are as follows:

1. The results of PDP and EIS show that the corrosion resistance of X100 in the produced water of saturated CO₂ oilfield decreases with the increase of the flow rate under simulated real conditions.
2. The increase of flow rate accelerated the corrosion degree of the samples, and the corrosion products accumulated more in the same corrosion time. And with the increase of the flow velocity, mass transfer will be enhanced, the steel matrix will dissolve continuously, and all the reaction will be continued, resulting in serious corrosion and high corrosion current density.
3. The flow regime is turbulent under simulated working conditions; at different locations, the flow condition is different, and with the aggregation effect of CO₂, the initiation point of corrosion easily occurred in the bend segment. The corrosion of the bend segment is more serious than that of the straight segment.
4. Pipeline corrosion failure in engineering is mostly caused by local corrosion, so the experimental results under simulated working conditions will have more guiding significance for engineering practice.

Funding The authors are recipients of the financial support from the Beijing Municipal Natural Science Foundation (Grant No. 3192013) and the National Natural Science Foundation of China (No. 51774046).

References

1. Rui Z, Cui K, Wang X, Lu J, Chen G (2018) A quantitative framework for evaluating unconventional well development. *J Pet Sci Eng* 166:900–905
2. Rui Z, Guo T, Feng Q, Qu Z, Qi N, Gong F (2018) Influence of gravel on the propagation pattern of hydraulic fracture in the glutenite reservoir. *J Pet Sci Eng* 165:627–639
3. Rui Z, Wang X, Zhang Z, Lu J, Chen G (2018) A realistic and integrated model for evaluating oil sands development with steam assisted gravity drainage technology in Canada. *Appl Energy* 213:76–91
4. Qian L-Y, Fang G, Zeng P, Wang L-X (2015) Correction of flow stress and determination of constitutive constants for hot working of API X100 pipeline steel. *Int J Press Vessel Pip* 132–133:43–51
5. Mahdi E, Rauf A, Eltai EO (2014) Effect of temperature and erosion on pitting corrosion of X100 steel in aqueous silica slurries containing bicarbonate and chloride content. *Corros Sci* 83:48–58
6. Jin TY, Cheng YF (2011) In situ characterization by localized electrochemical impedance spectroscopy of the electrochemical activity of microscopic inclusions in an X100 steel. *Corros Sci* 53(2):850–853
7. Okonkwo P, Shakoor R, Benamor A, Amer Mohamed A, Al-Marri M (2017) Corrosion behavior of API X100 steel material in a hydrogen sulfide environment. *Metals* 7(4):109
8. Zhang GA, Zeng L, Huang HL, Guo XP (2013) A study of flow accelerated corrosion at elbow of carbon steel pipeline by array electrode and computational fluid dynamics simulation. *Corros Sci* 77:334–341
9. Islam MA, Farhat Z (2017) Erosion-corrosion mechanism and comparison of erosion-corrosion performance of API steels. *Wear* 376–377:533–541
10. Malka R, Nešić S, Gulino DA (2007) Erosion–corrosion and synergistic effects in disturbed liquid-particle flow. *Wear* 262(7–8):791–799
11. Xu G, Cai L, Ullmann A, Brauner N (2016) Experiments and simulation of water displacement from lower sections of oil pipelines. *J Pet Sci Eng* 147(Supplement C):829–842
12. Sun G, Zhang J, Ma C, Wang X (2016) Start-up flow behavior of pipelines transporting waxy crude oil emulsion. *J Pet Sci Eng* 147(Supplement C):746–755
13. Zhang GA, Liu D, Li YZ, Guo XP (2017) Corrosion behaviour of N80 carbon steel in formation water under dynamic supercritical CO₂ condition. *Corros Sci* 120:107–120
14. Zhang GA, Zeng Y, Guo XP, Jiang F, Shi DY, Chen ZY (2012) Electrochemical corrosion behavior of carbon steel under dynamic high pressure H₂S/CO₂ environment. *Corros Sci* 65(12):37–47
15. Utanohara Y, Murase M (2019) Influence of flow velocity and temperature on flow accelerated corrosion rate at an elbow pipe. *Nucl Eng Des* 342:20–28
16. Liu AQ, Bian C, Wang ZM, Han X, Zhang J (2018) Flow dependence of steel corrosion in supercritical CO₂ environments with different water concentrations. *Corros Sci* 134:149–161
17. Ajmal TS, Arya SB, Udupa KR (2019) Effect of hydrodynamics on the flow accelerated corrosion (FAC) and electrochemical impedance behavior of line pipe steel for petroleum industry. *Int J Press Vessel Pip* 174:42–53
18. Liu T, Cheng YF, Sharma M, Voordouw G (2017) Effect of fluid flow on biofilm formation and microbiologically influenced corrosion of pipelines in oilfield produced water. *J Pet Sci Eng* 156:451–459
19. Galvan-Martinez R, Mendoza-Flores J, Duran-Romero R, Genesca-Llongueras J (2004) Effects of turbulent flow on the corrosion kinetics of X52 pipeline steel in aqueous solutions containing H₂S. *Mater Corros* 55(8):586–593
20. Oliveira ESD, Pereira RFC, Melo IR, Lima MAGA, Urtiga Filho SL (2017) Corrosion behavior of API 5L X80 steel in the produced water of onshore oil recovery facilities. *Mater Res* 20(suppl 2):432–439
21. Kahyarian A, Brown B, Nescic S (2017) Electrochemistry of CO₂ corrosion of mild steel: effect of CO₂ on iron dissolution reaction. *Corros Sci* 129:146–151
22. Kahyarian A, Schumaker A, Brown B, Nescic S (2017) Acidic corrosion of mild steel in the presence of acetic acid: mechanism and prediction. *Electrochim Acta* 258:639–652

23. Obot IB, Onyechu IB, Umoren SA (2019) Alternative corrosion inhibitor formulation for carbon steel in CO₂-saturated brine solution under high turbulent flow condition for use in oil and gas transportation pipelines. *Corros Sci* 159:108140
24. Ruiz-Luna H, Porcayo-Calderón J, Mora-García AG, López-Báez I, Martínez-Gomez L, Muñoz-Saldaña J (2019) Corrosion performance of AISI 304 stainless steel in CO₂-saturated brine solution. *Prot Met Phys Chem Surf* 55(6):1226–1235
25. Majchrowicz K, Brynk T, Wiczorek M, Miedzińska D, Pakiela Z (2019) Exploring the susceptibility of P110 pipeline steel to stress corrosion cracking in CO₂-rich environments. *Eng Fail Anal* 104: 471–479
26. Zhou S, Rabczuk T, Zhuang X (2018) Phase field modeling of quasi-static and dynamic crack propagation: COMSOL implementation and case studies. *Adv Eng Softw* 122:31–49
27. Song X, Yang Y, Yu D, Lan G, Wang Z, Mou X (2016) Studies on the impact of fluid flow on the microbial corrosion behavior of product oil pipelines. *J Pet Sci Eng* 146:803–812
28. Thaker J, Banerjee J (2016) Influence of intermittent flow sub-patterns on erosion-corrosion in horizontal pipe. *J Pet Sci Eng* 145:298–320
29. Wu JW, Bai D, Baker AP, Li ZH, Liu XB (2015) Electrochemical techniques correlation study of on-line corrosion monitoring probes. *Mater Corros* 66(2):143–151
30. Richter S, Hilbert LR, Thorarinsdottir RI (2006) On-line corrosion monitoring in geothermal district heating systems. I. General corrosion rates. *Corros Sci* 48(7):1770–1778
31. Richter S, Thorarinsdottir RI, Jonsdottir F (2007) On-line corrosion monitoring in geothermal district heating systems. II. Localized corrosion. *Corros Sci* 49(4):1907–1917
32. Zhao J, Xiong D, Gu Y, Zeng Q, Tian B (2018) A comparative study on the corrosion behaviors of X100 steel in simulated oilfield brines under the static and dynamic conditions. *J Pet Sci Eng* 173: 1109–1120
33. Mohammadi F, Eliyan FF, Alfantazi A (2012) Corrosion of simulated weld HAZ of API X-80 pipeline steel. *Corros Sci* 63(Supplement C):323–333
34. Ha HM, Gadala IM, Alfantazi A (2016) Hydrogen evolution and absorption in an API X100 line pipe steel exposed to near-neutral pH solutions. *Electrochim Acta* 204(Supplement C):18–30
35. Eliyan FF, Mohammadi F, Alfantazi A (2012) An electrochemical investigation on the effect of the chloride content on CO₂ corrosion of API-X100 steel. *Corros Sci* 64:37–43
36. Eliyan FF, Alfantazi A (2014) On the theory of CO₂ corrosion reactions – investigating their interrelation with the corrosion products and API-X100 steel microstructure. *Corros Sci* 85:380–393
37. Gao M, Pang X, Gao K (2011) The growth mechanism of CO₂ corrosion product films. *Corros Sci* 53(2):557–568
38. Cui ZD, Wu SL, Zhu SL, Yang XJ (2006) Study on corrosion properties of pipelines in simulated produced water saturated with supercritical CO₂. *Appl Surf Sci* 252(6):2368–2374
39. Robinson DF, Hassan HA (1998) Two-equation turbulence closure model for wall bounded and free shear flows. *AIAA J* 36(1):109–111
40. Wilcox DC (1992) Dilatation-dissipation corrections for advanced turbulence models. *AIAA J* 30(11):2639–2646
41. Tan ZW, Zhang DL, Yang LY et al (2020) Development mechanism of local corrosion pit in X80 pipeline steel under flow conditions. *Tribol Int* 146:106145

Publisher's note Springer Nature remains neutral with regard to jurisdictional claims in published maps and institutional affiliations.